Interaction between trefoil knotted flame and vortex

Yunde Su (苏运德)
State Key Laboratory for Turbulent and Complex Systems, College of Engineering, Peking University, Beijing 100871, China

Yue Yang (杨越)*
State Key Laboratory for Turbulent and Complex Systems, College of Engineering, Peking University, Beijing 100871, China and HEDPS-CAPT, Peking University, Beijing 100871, China

(Received 6 April 2023; accepted 17 November 2023; published 5 December 2023)

We study the interaction between knotted flame and vortex tubes using the direct numerical simulation. A 3D configuration of the flame-vortex interaction is proposed. The premixed flame is initially located within a vortex tube with the same trefoil knotted centerline, and it propagates outward and interacts with the knotted vortex tube. This configuration is able to investigate the flame extinction, flame-flame interaction, and suppression of the vortex reconnection. Compared to the nonreacting knotted vortex tube, the flame-vortex interaction modifies the helicity dynamics and the morphology of vortex and flame tubes. The combustion generally decreases the helicity due to enhanced viscosity effects, but also slightly increases the helicity during a short time when the local extinction occurs. The nonmonotonic variation of the helicity results from the unsymmetrical flame propagation along the vortex axis after the local flame extinction. Moreover, some parts of the flame and vortex tubes are flattened through the early evolution. The flattening is primarily due to the baroclinic effects arising from the misalignment between the local density gradient and the nonlocal pressure gradient that strongly depends on the flame-vortex configuration.

DOI: 10.1103/PhysRevFluids.8.123201

I. INTRODUCTION

The interaction between the premixed flame and turbulence is of great interest in engineering applications, such as internal combustion engines and lean-burn gas turbines. The flame modifies the turbulent flow by the heat release, and the vortical flow wrinkles and folds the flame to enhance combustion or cause local extinction. To date, the direct numerical simulation (DNS) and experimental studies of turbulent premixed combustion under practical operating conditions remain challenging. As a simplified model problem, the interaction of the premixed flame and the vortex with prescribed vortex size and intensity has been extensively employed to study the effect of heat release on vortical flow [1] and the effect of vortical flow on flame propagation and combustion [2–5]. These studies were also used to develop and examine predictive models relevant to turbulent combustion [6–8].

Most existing works on the flame-vortex interaction focused on 2D configurations, where a pair of counter-rotating vortices or a single vortex move towards a freely propagating planar flame. However, such a simplification cannot capture the essential vortex dynamics in 3D turbulent flows, e.g., vortex stretching, twisting [9,10], and reconnection [11,12]. Thus, we need to develop 3D

*yyg@pku.edu.cn

configurations for flame-vortex interaction, which should be relatively simple and capture the major features in turbulent combustion. Zhou *et al.* [13] studied the interaction between the premixed flame and 3D Taylor-Green vortex. They found that the laminar-turbulent transition is suppressed in the burned region, and the vorticity magnitude near the flame front can be augmented.

The knot, a curve in 3D space, can characterize a vortex tube with nontrivial topology [14]. The feasible method for constructing complex knotted vortex tubes [15,16] has been employed to study the dynamics of knotted and linked vortex tubes [17–19], which is useful in understanding the energy cascade in turbulent flows [12]. It is straightforward to extend the construction method to studying the interaction between knotted flame and vortex in 3D space.

The topology of a knotted field can be measured by the helicity [20,21], one of the two quadratic invariants in ideal flows (the other is the kinetic energy). Although the helicity is important in the energy cascade and coherent structures in turbulent flows [22–25], little work has been performed in studying the helicity dynamics in turbulent combustion. Recently, the helicity density was used to quantify the interaction of toroidal vortices in triple flickering buoyant diffusion flames [26]. The effects of combustion on the helicity in variable-density reactive flows, however, remain to be investigated.

The morphology also characterizes the flame-vortex interaction. The morphology of flow structures sheds light on the energy cascade in turbulence. The vortical structures were shown to migrate from bloblike to sheetlike structures with decreasing length scales [27–29]. The morphology of flames is of importance in studying the physics of turbulent combustion [30–32] and developing predictive models [33–35]. The studies of flame morphology found the hydrodynamic instability causes sharp folds and creases [36], the thermal-diffusive instability enhances cellular structures and distinct cusps [32,37], and the flame-flame interaction causes the pocket formation [38,39]. In terms of flame-vortex interaction, Minamoto *et al.* [40] argued that the length scales greater than the Taylor scale are responsible for the flame shape via the morphology analysis of hydrogen-air turbulent premixed flames. Moreover, the fractal properties of flames have been widely used to model the turbulent flame speed in large-eddy simulation of turbulent flames with the flamelet assumption [7,41,42]. On the other hand, the existing studies on the flame morphology focused on the statistical analysis of turbulent flames. The detailed flame-vortex interaction needs to be elucidated using the morphology analysis in a simple 3D configuration.

In the present paper, we develop a 3D configuration of the flame-vortex interaction by extending the knot construction method [15]. The knotted vortex and flame tubes are initially placed along the same tube centerline. They evolve and interact with each other. We demonstrate the effects of combustion on helicity dynamics and analyze the flame (vortex) morphology with an emphasis on the baroclinic effect.

The rest of this paper is organized as follows. The 3D configuration of the flame (vortex) knot and the DNS are presented in Sec. II. In Sec. III, the evolutions of vortex and flame tubes with different initial conditions are compared, followed by the analysis of the helicity dynamics focusing on the flame propagation and morphology of flame and vortex tubes. Some conclusions are drawn in Sec. IV.

II. SIMULATION OVERVIEW

A. Initial configuration of knotted vortex and flame tubes

We construct knotted vortex and flame tubes by extending the method of Xiong and Yang [15,16]. The initial centerline $\mathcal{C}$ of the vortex and flame tubes is a trefoil torus knot, lying on the surface of an unknotted torus in $\mathbb{R}^3$. The parametric equations of $\mathcal{C}$ are

$$\begin{aligned} c_x(\zeta) &= c_{x0} + (R_t + r_t\cos(q\zeta))\cos(p\zeta) \\ c_y(\zeta) &= c_{y0} + (R_t + r_t\cos(q\zeta))\sin(p\zeta) \\ c_z(\zeta) &= c_{z0} - r_t\sin(q\zeta), \end{aligned} \tag{1}$$

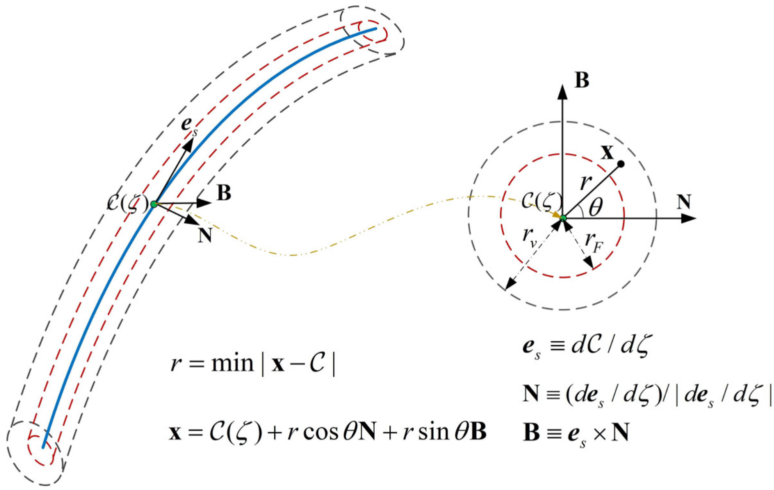

FIG. 1. Schematic of the curved cylindrical coordinate system. The flame and vortex tubes are marked by the dashed red and grey lines, respectively. The centerline is marked by the blue solid curve.

where $[c_{x0}, c_{y0}, c_{z0}]$ denotes the centerline location, $\zeta \in [0, 2\pi)$ the parameter, and R_t and r_t the major and minor radii of the torus, respectively. The torus knot $\mathcal{C}$ winds q times around a circle in the interior of the torus and p times around its axis of rotational symmetry.

Based on the centerline $\mathcal{C}$, the vorticity of the vortex tube in the curved cylindrical coordinate system (s, r, θ) is constructed as [43]

$$\boldsymbol{\omega}(s, r, \theta) = \Gamma f(r)\boldsymbol{e}_s, \tag{2}$$

where Γ is the strength of the vorticity flux along $\mathcal{C}$, $\boldsymbol{e}_s$ denotes the axial unit vector of $\mathcal{C}$, and the coordinates (s, r, θ) are sketched in Fig. 1. The flux distribution

$$f(r) = \frac{1}{2\pi\sigma^2}\exp\left(-\frac{r^2}{2\sigma^2}\right) \tag{3}$$

is set to be Gaussian with the standard deviation σ. The radius $r_v = 2\sigma$ of the vortex tube is estimated [19,44].

The knotted flame tube has the same centerline $\mathcal{C}$ of the vortex tube. The initial species distribution is set as

$$Y_i(x, y, z) = \frac{1}{2}\left(\tanh\left(\frac{r_F - r}{\delta}\right) + 1\right)\left(Y_i^u - Y_i^b\right) + Y_i^b, \tag{4}$$

where r_F is the radius of the flame tube, δ a parameter for setting the initial flame thickness, and Y_i^u and Y_i^b the unburned and burned species mass fraction, respectively.

As initial conditions of DNS, $\boldsymbol{\omega}$ and Y_i for the vortex and flame tubes are constructed in a periodic box. Then the initial velocity is calculated from $\boldsymbol{\omega}$ by the Biot-Sarvart law in Fourier space [15].

Figure 2 shows the initial configuration of the trefoil knotted flame and vortex tubes with $(p, q) = (2, 3)$. In this configuration, the flame tube expands outward, and the vortex tube warping the flame tube evolves under the influence of self-induction and combustion. We also examined the opposite condition where the initial flame warps the vortex tube and propagates inward. The flame evolution is so intensive and rapid that it burns out in a short time, and thus this configuration is not considered.

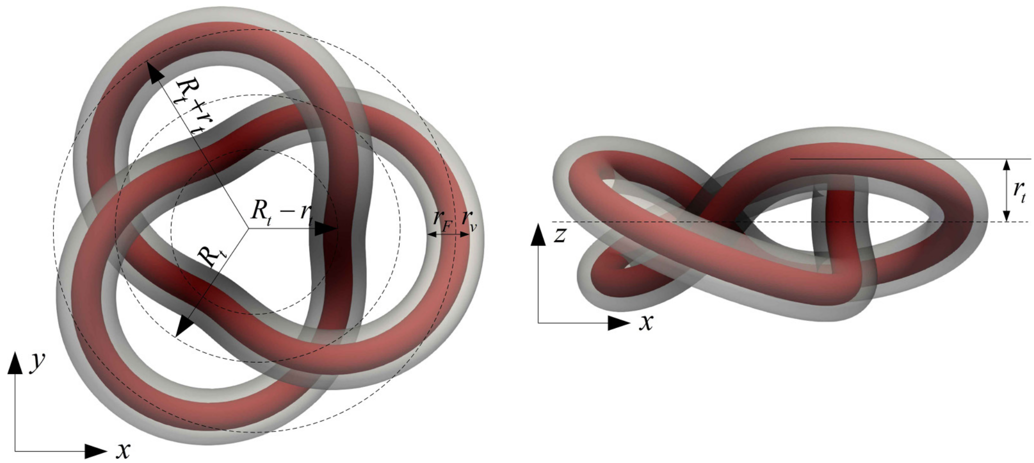

FIG. 2. Initial configuration (red: flame front; grey: isosurface of vortex tube).

B. DNS

In the present DNS, the chemistry is simplified using the one-step assumption. The one-step chemistry captures the effects of combustion heat release on the flow and has been extensively used in the DNS of premixed turbulent combustion [37,45,46]. With the assumptions of the one-step chemistry, low Mach number, Fick's diffusion law, equal heat capacity, unity Lewis number, and adiabatic condition, the thermal-chemical state is represented by the progress variable

$$c \equiv 1 - \frac{Y_F}{Y_F^u} = \frac{T - T_u}{T_b - T_u}, \tag{5}$$

where Y_F represents the fuel mass fraction, Y_F^u the fuel mass fraction in the unburned state, T the temperature, and T_b and T_u the temperature in the burned and unburned state, respectively.

With these simplifications, the reactive vortical flow is described by the continuity equation

$$\frac{\partial \rho}{\partial t} + \frac{\partial \rho u_j}{\partial x_j} = 0, \tag{6}$$

the momentum equation

$$\frac{\partial \rho u_i}{\partial t} + \frac{\partial \rho u_j u_i}{\partial x_j} = -\frac{\partial P}{\partial x_i} + \frac{\partial \tau_{ij}}{\partial x_j}, \tag{7}$$

and the transport equation of c,

$$\frac{\partial \rho c}{\partial t} + \frac{\partial \rho u_j c}{\partial x_j} = \frac{\partial}{\partial x_j}\left(\rho D_F \frac{\partial c}{\partial x_j}\right) + \rho\dot{\omega}, \tag{8}$$

where ρ denotes the density, u_i the velocity, P the pressure, and τ_{ij} the viscous stress tensor. The molecular mass diffusivity $D_F = D_F^0 (T/T_u)^{0.76}$ is evaluated by the temperature, where D_F^0 is the mass diffusivity at the unburned temperature.

The reaction source term $\dot{\omega} = A(1-c)\exp(-E_a/RT)$ is modeled by the single-step Arrhenius-type chemistry, where A is the pre-exponential factor, E_a the activation energy, and R the gas constant. The density is evaluated as

$$\frac{1}{\rho} = [(1-c)/\rho_u + c/\rho_b]\left[\int \frac{1}{(1-c)/\rho_u + c/\rho_b} dV\right]\frac{1}{M}, \tag{9}$$

TABLE I. DNS parameters, where L is the length of the computational domain.

	Case 1	Case 2	Case 3
(p, q)	(2,3)	(2,3)	(2,3)
r_t/R_t	0.42	0.42	0.42
R_t/L	0.19	0.19	0.19
r_v/r_F		2.44	2.44
r_v/L	0.048	0.048	0.048
r_F/δ_l		1	1
$\mathrm{Re} = \Gamma/\nu$	2000	2000	2000
Equivalence ratio ϕ		0.55	0.65
$\mathrm{Da} = (R_t^2/\Gamma)/(\delta_l/S_L)$	∞	0.28	0.31
Da^*		0.36	0.36
N	1024	1024	1024

where ρ_u and ρ_b are the unburned and burned densities, respectively, at the initial thermal state, M denotes the constant mass in the computational domain, and $\int 1/[(1-c)/\rho_u + c/\rho_b]dV/M$ is used to correct the variation of the thermal pressure. The influence of the thermal pressure on the chemistry parameters is neglected due to the small variation of the thermal pressure [47].

The simulation is performed using the code NGA [48] for low-Mach-number, variable density flows, which has been widely used in DNS of turbulent combustion [35,37,47,49,50]. The governing equations are discretized on a staggered mesh using the hybrid finite difference scheme [48,51]. The convective terms in the continuity and the momentum equations are discretized with the second-order conservative central difference scheme. The convective term in the scalar transport equation is discretized using the fifth-order WENO scheme [52]. The pressure-gradient, viscous term, and the diffusion terms are discretized using second-order central schemes. The semi-implicit second-order Crank-Nicholson scheme is used for time integration [53].

We performed two reactive and one nonreactive DNS cases. Their parameters are listed in Table I. In the three cases, the Reynolds number (Re) and the normalized geometrical parameters are kept the same. In the reactive cases, the unburned mixture at the initial state is chosen as the lean methane-air with the equivalence ratio $\phi = 0.55$ and 0.65, respectively. The burned densities at the initial state are evaluated from the unburned mixture. We adjusted A, E_a, and the kinematic viscosity ν so the laminar flame speed S_L, the thermal flame thickness δ_l, and the Zeldovich number Ze are matched with the simulation results obtained using the detailed chemistry. In Eq. (4), $\delta = 0.13\delta_l$ is set so local extinction can be observed. The influence of the initial flame thickness on the simulation results is discussed in Appendix A. The nonreactive case without flame propagation and heat release effects is used to compare with the reactive cases to highlight the effect of flame-vortex interactions. All simulations are performed in a periodic box with $N^3 = 1024^3$ grid points over a period of ten characteristic times of the vortex evolution. The Courant-Friedrichs-Lewy number is set to 0.5. As demonstrated in Appendix B, the grid resolution is sufficient to resolve the vorticity evolution and flame propagation.

The characteristic time of the vortex evolution is defined as [17]

$$t_v = R_t^2/\Gamma, \tag{10}$$

with the parameters of the initial knotted vortex tube. The characteristic time of the flame propagation can be

$$t_F = \delta_l/S_L. \tag{11}$$

We define a Damköhler number

$$\mathrm{Da} = t_v/t_F = \left(R_t^2/\Gamma\right)/(\delta_l/S_L) \tag{12}$$

as the ratio of strengths of the vortex evolution and flame propagation, and a characteristic Damköhler number:

$$\mathrm{Da}^* = \left(\frac{r_v}{r_F} - 1\right)\frac{r_F}{\delta_l}/\hat{t}^*. \tag{13}$$

Here,

$$\hat{t}^* = \hat{t}/t_v \tag{14}$$

is a normalized reconnection time of the vortex tube depending on the specific knot configuration, where $\hat{t}$ is the time when the reconnection occurs, and Da^* is the critical Da characterizing that the flame collides with the vortex tube at $\hat{t}$. For Eq. (13), it is assumed that the variation of S_L is small, and S_L is much larger than the growth rate of the vortex core due to viscosity. The comparison between Da and Da^* measures the relative speed of flame propagation and vortex reconnection.

The flame propagation and vortex reconnection are two major events in the early evolution. The former dominates the latter when $\mathrm{Da} \ll \mathrm{Da}^*$ as the flame moves much faster than the vortex tubes, whereas the vortex reconnection dominates over the flame propagation when $\mathrm{Da} \gg \mathrm{Da}^*$. This timescale analysis is used to set up a physically interesting configuration of knotted vortex and flame tubes. In the reactive cases, with $r_v/r_F = 2.44$, $r_F/\delta_l = 1$, and $\hat{t}^* \approx 4$, Da^* is around 0.36. As shown in Table I, Da in both cases is close to Da^*, suggesting that both the flame propagation and vortex evolution can play important roles in 3D flame-vortex interactions.

Note that although the initial divergence-free velocity field calculated from Eq. (2) does not satisfy the continuity equation in the reacting cases, the effect of this numerical artifact on the total helicity and enstrophy is negligibly small and is rapidly suppressed before $t^* = 0.1$.

III. RESULTS

A. Evolution of vortex and flame tubes

Figure 3 depicts the temporal evolution of isosurfaces of the vorticity magnitude $|\boldsymbol{\omega}|$, where the surfaces are color-coded by the helicity density $h \equiv \boldsymbol{u} \cdot \boldsymbol{w}$, and the time $t^* = t/t_v$ is normalized. The vorticity and the helicity are normalized as $\boldsymbol{\omega}^* = \boldsymbol{\omega} R_t^2/\Gamma$ and $h^* = hR_t^3/\Gamma^2$, respectively. In all three cases, the neighboring parts of the vortex tube tend to be antiparallel, and then collide with each other around $t^* = 4$. In the nonreactive case, the vortex tube has reconnection, generating bridges and threads. Compared to previous observations [17,54], the helical structures after reconnection are not obvious in the present nonreactive case due to the smaller Re and the larger vortex radius. The bridges and threads in the reactive cases are suppressed due to the enhanced dissipation by combustion. Moreover, the inner (with smaller radius to the centerline) portion of the vortex tubes is gradually flattened in the reactive cases, which will be elaborated upon in Sec. III C, and the maximum helicity density decreases more rapidly in the reactive cases than in the nonreactive case.

Figure 4 highlights the flame propagation (red surfaces), along with the vortex evolution (translucent surfaces) in the reactive cases. The flame front is represented by the isosurface of $c = 0.8$, where the reaction rate is close to half the maximum value in the unstretched planar laminar flame [37,55]. The flame propagates outward and finally moves outside of the vortex tube defined by $|\boldsymbol{\omega}^*| = 1$ after $t^* = 6$. During this process, the flame propagation is strongly affected by the vortex evolution and vice versa. Both the flame and vortex tubes are flattened. In particular, the flame extinction and the flame-flame interaction are observed. The extinction occurs in the leaner flame with $\phi = 0.55$ due to the greater sensitivity to flame stretching induced by the vortical flow. The flame-flame interaction occurs when the separated flame tubes reunite after the local extinction and when the flame tubes collide with each other due to vortex induction.

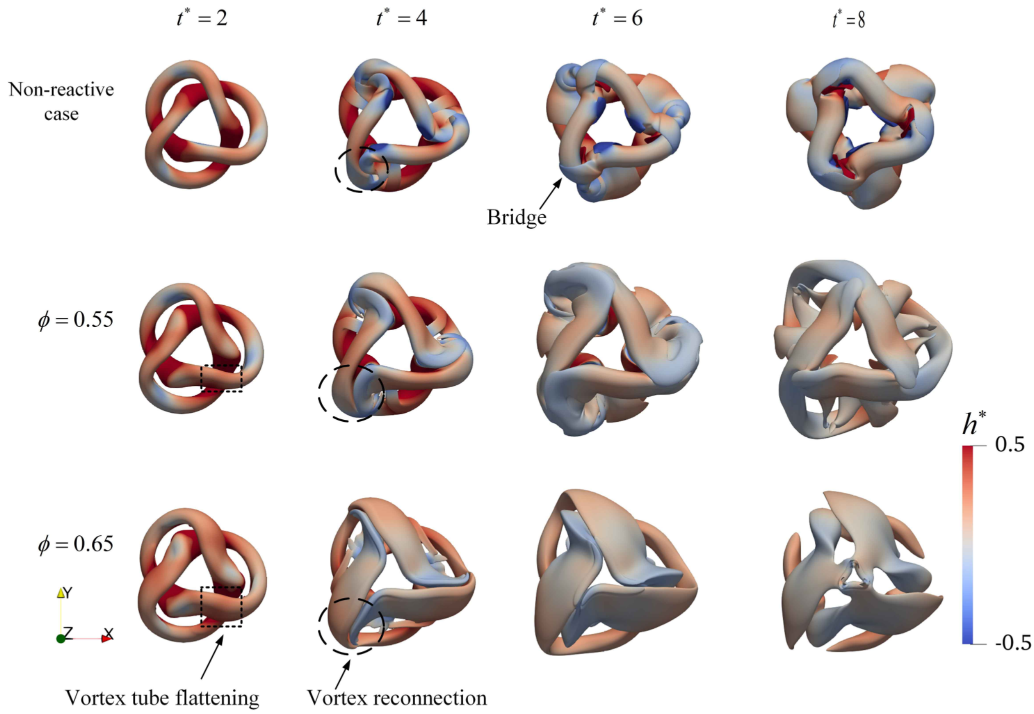

FIG. 3. Evolution of vortex structures represented by isosurfaces of $|\boldsymbol{\omega}^*| = 2$ for $t^* = 2$, $|\boldsymbol{\omega}^*| = 1.5$ for $t^* = 4$, and $|\boldsymbol{\omega}^*| = 1$ for $t^* = 6$ and 8. The surfaces are color-coded by h^*.

B. Helicity dynamics

Figure 5 plots the temporal evolution of the total helicity $H \equiv \int h\, dV$ and of the total enstrophy $E_\Omega \equiv \int \Omega\, dV$ with $\Omega \equiv |\boldsymbol{\omega}|^2/2$ over the computational domain. In the nonreactive case, H generally

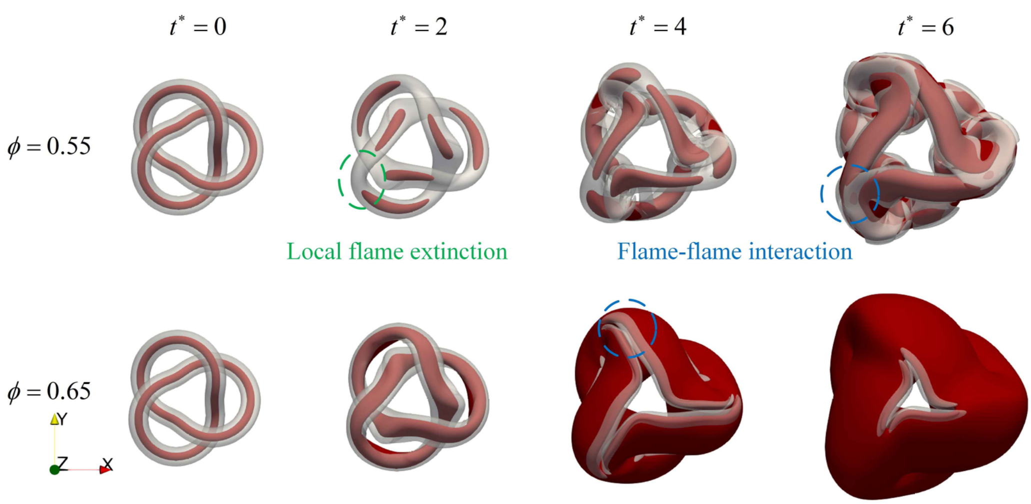

FIG. 4. Evolution of flame fronts represented by isosurfaces of $c = 0.8$ (red) and vortex structures represented by isosurfaces of $|\boldsymbol{\omega}^*|$ (grey). The isocontour values of $|\boldsymbol{\omega}^*|$ are the same as in Fig. 3.

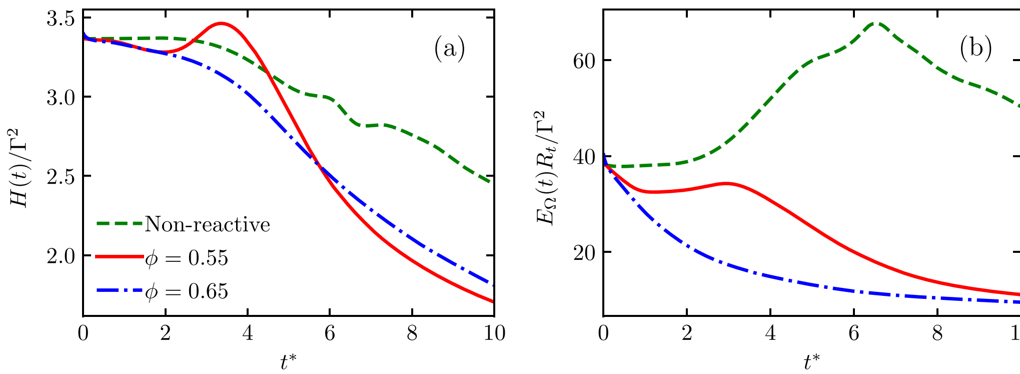

FIG. 5. Evolution of (a) the total helicity and (b) the enstrophy.

decreases with time, consistent with the contour color of h shown in Fig. 3. There are local mild oscillations of H around $t^* = 6$, accompanied with the rise of E_Ω. These observations result from the reconnection that causes the enhanced stretch and the generation of the helicity and enstrophy. Compared with previous results [17,54], there is no sharp rise of H, because the present reconnection is weaker with larger vortex radius and smaller Re. In general, both H and E_Ω in the reactive cases decrease more rapidly than in the nonreactive case due to the enhanced viscosity resulting from the heat release in combustion. On the other hand, the profile of $H(t)$ shows a peak around $t^* = 3$ in the reactive case with $\phi = 0.55$, which will be explained below.

1. Governing equation of the helicity

To study the influence of combustion on helicity dynamics, we derive and analyze the governing equation of H. The governing equation of h is derived from the momentum equation [Eq. (7)] as

$$\frac{\partial h}{\partial t} = \underbrace{-u_j\frac{\partial h}{\partial x_j}}_{\text{Conv}} \underbrace{-h\frac{\partial u_j}{\partial x_j}}_{\text{Dila}} + \underbrace{\omega_j\frac{\partial}{\partial x_j}\left(\frac{1}{2}u_iu_i\right)}_{\text{KEgrad}}$$
$$+ \underbrace{\frac{1}{\rho^2}u_i\varepsilon_{ijk}\frac{\partial \rho}{\partial x_j}\frac{\partial P}{\partial x_k}}_{\text{Baro}} \underbrace{-\frac{1}{\rho}\omega_j\frac{\partial P}{\partial x_j}}_{\text{Pgrad}} + \underbrace{\frac{1}{\rho}\omega_i\frac{\partial \tau_{ij}}{\partial x_j}}_{\text{Visc1}} + \underbrace{\varepsilon_{ijk}u_i\frac{\partial}{\partial x_j}\left(\frac{1}{\rho}\frac{\partial \tau_{km}}{\partial x_m}\right)}_{\text{Visc2}}. \tag{15}$$

The shorthand name for each term is marked under each one.

We analyze and rearrange the terms in Eq. (15) to simplify the governing equation of H. First, the convective and dilatation terms

$$\text{Conv} + \text{Dila} = -u_j\frac{\partial h}{\partial x_j} - h\frac{\partial u_j}{\partial x_j} = -\frac{\partial hu_j}{\partial x_j} \tag{16}$$

are added in a divergence form. Second, the term

$$\text{KEgrad} = \omega_j\frac{\partial}{\partial x_j}\left(\frac{1}{2}u_iu_i\right) = \frac{\partial}{\partial x_j}\left(\frac{1}{2}u_iu_i\omega_j\right) \tag{17}$$

is also reexpressed in a divergence form using the identity $\partial\omega_i/\partial x_i = 0$. Third, the volume integrations of the baroclinic torque and pressure gradient terms are the same due to

$$\text{Baro} - \text{Pgrad} = \frac{1}{\rho^2}u_i\varepsilon_{ijk}\frac{\partial \rho}{\partial x_j}\frac{\partial P}{\partial x_k} + \frac{1}{\rho}\omega_j\frac{\partial P}{\partial x_j} = \nabla\cdot\left(-\frac{\nabla P}{\rho}\times \boldsymbol{u}\right) \tag{18}$$

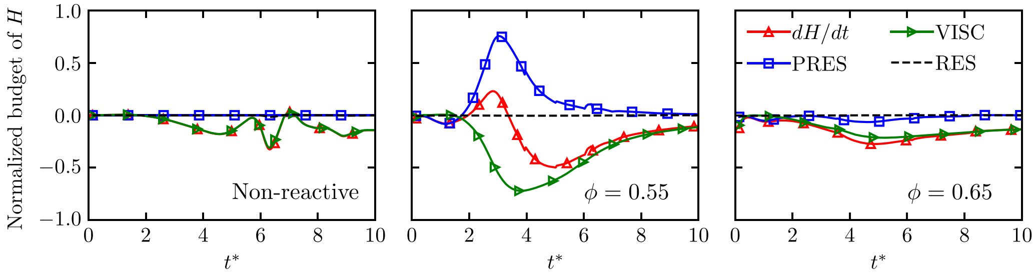

FIG. 6. Helicity budgets and the residual RES $= dH/dt - (\text{PRES} + \text{VISC})$ in different DNS cases.

and the divergence theorem. Forth, the volume integrations of the two viscous terms are also the same due to

$$\text{Visc1} - \text{Visc2} = \frac{1}{\rho}\omega_i \frac{\partial \tau_{ij}}{\partial x_j} - \varepsilon_{ijk} u_i \frac{\partial}{\partial x_j}\left(\frac{1}{\rho}\frac{\partial \tau_{km}}{\partial x_m}\right) = \varepsilon_{ijk}\frac{\partial}{\partial x_j}\left(\frac{1}{\rho}\frac{\partial \tau_{ij}}{\partial x_j} u_k\right). \tag{19}$$

Applying the volume integration to Eq. (15) and simplifying the integrated equation using Eqs. (16)–(19), we obtain the governing equation of H in a variable-density flow in a periodic box as

$$\frac{dH}{dt} = \underbrace{\int \left(-2\frac{1}{\rho}\omega_j \frac{\partial P}{\partial x_j}\right) dV}_{\text{PRES}} + \underbrace{\int \left(2\frac{1}{\rho}\omega_i \frac{\partial \tau_{ij}}{\partial x_j}\right) dV}_{\text{VISC}}. \tag{20}$$

Compared with the governing equation of H in incompressible flows, there is an additional term PRES related to the pressure gradient (or baroclinic effects) in Eq. (20). This term arises due to the variable density and can be significantly influenced by the heat release in combustion. Additionally, the viscous term VISC in Eq. (20) can also be affected by combustion due to the temperature-dependence of the viscosity.

2. *Helicity budget*

Figure 6 plots the budgets of H, normalized by Γ^3/R_t^2. The budget residual is negligible in all three cases. In the nonreactive case, pressure-related terms (Baro + Pgrad) in Eq. (20) are vanishing as expected, and the variation of H is governed by viscous terms. The oscillations of viscous terms during $4 < t^* < 8$ correspond to the vortex reconnection shown in Fig. 3. In the reactive cases, the variation of H is affected by both pressure-related and viscous terms. As the vortex reconnection is suppressed, the oscillations of viscous terms diminish.

For $\phi = 0.55$, the positive peak of the pressure term occurs earlier than the negative peak of the viscous term. This causes the nonmonotonic variation of H near $t^* = 3$ [see Fig. 5(a)]. Then, the viscous term dominates the decay of H. Compared to the case with $\phi = 0.55$, term PRES is much weaker with $\phi = 0.65$, so the evolution of H is mainly controlled by term VISC, without showing the nonmonotonic variation. In addition, the weak local oscillations in the evolution of PRES in the case with $\phi = 0.65$ result from the variation of the local pressure during flame-flame interactions.

3. *Helicity generation and flame propagation*

We explain the rise of H in the case with $\phi = 0.55$ during the vortex reconnection by analyzing the pressure-related term in Eq. (15). Implied by Eq. (18), the integrations of terms Baro and Pgrad are equal, so we only analyze the pressure-gradient term via the decomposition

$$\int \text{Pgrad}\; dV = \int \text{Pgrad}^+\; dV + \int \text{Pgrad}^-\; dV, \tag{21}$$

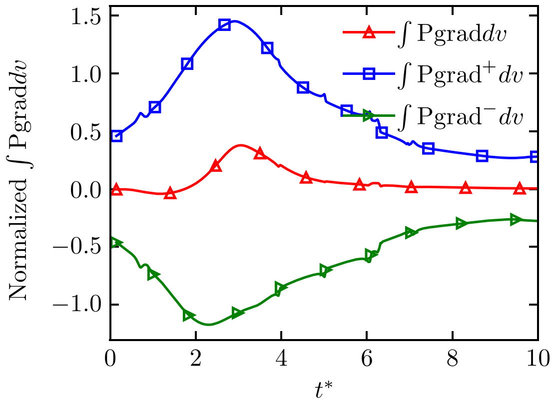

FIG. 7. Evolution of the decomposed and normalized pressure-gradient terms of the total helicity budgets in the case with $\phi = 0.55$.

with

$$\mathrm{Pgrad}^+ = \begin{cases} \mathrm{Pgrad}, & \text{if} \quad \mathrm{Pgrad} \geqslant 0 \\ 0, & \text{otherwise} \end{cases}, \tag{22}$$

and $\mathrm{Pgrad}^- = \mathrm{Pgrad} - \mathrm{Pgrad}^+$.

Figure 7 shows the evolution of the decomposed and normalized pressure-gradient terms for $\phi = 0.55$. Magnitudes of both $\int \mathrm{Pgrad}^+ \, dV$ and $\int \mathrm{Pgrad}^- \, dV$ grow at early times and then decay. The sum of the two terms, $\int \mathrm{Pgrad} \, dV$, shows the same trend with a peak near $t^* = 3$. Therefore, the generation of H by pressure-related terms can be analyzed through either Pgrad^+ or Pgrad^-.

To elucidate the growth of H for $\phi = 0.55$, Fig. 8 compares the distributions of the term $\mathrm{Pgrad}^* = \mathrm{Pgrad}(R_t^5/\Gamma^3)$ for $\phi = 0.55$ and $\phi = 0.65$ at $t^* = 3$. We observe that bulks of both positive (green) and negative (blue) Pgrad are generated around the separated flame bulges caused by the local extinction for $\phi = 0.55$. In contrast, the generation of Pgrad^+ and Pgrad^- is suppressed for $\phi = 0.65$ without the extinction.

This comparison suggests a link between the helicity generation and flame evolution. As sketched in Fig. 9, the flame tip propagates along the vortex centerline (or vortex axis [56]) after the local extinction. The pressure gradient caused by the heat release is perpendicular to the curved flame

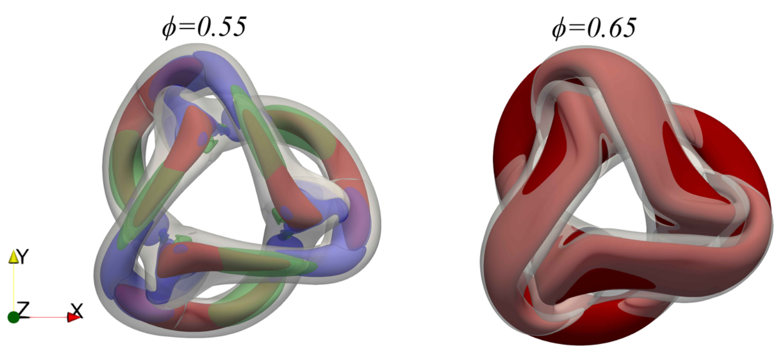

FIG. 8. Normalized pressure-related term of the helicity density budgets in the reactive vortex tubes at $t^* = 3$ (green: isosurface of $\mathrm{Pgrad}^* = 0.5$; blue: isosurface of $\mathrm{Pgrad}^* = -0.5$; red: isosurface of $c = 0.8$ (flame front); grey: isosurface of $|\boldsymbol{\omega}^*| = 1.5$).

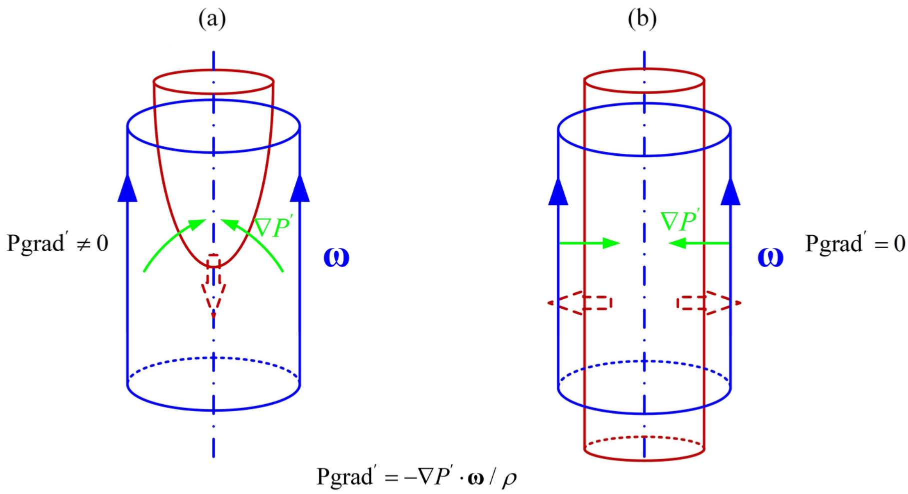

FIG. 9. Schematic of the helicity generation mechanism via flame propagation, where $\nabla P'$ denotes the pressure gradient due to flame propagation. The flame front and the vortex tubes are sketched by the red and blue lines, respectively. The vortex axis is marked by the dash-dotted blue line. The major directions of flame propagation are marked by the red dashed arrows. (a) Flame propagation along vortex axis and (b) Flame propagation normal to vortex axis.

front. This nonorthogonality of the pressure gradient and the vorticity generates the nonzero Pgrad. In particular, the flow field and the flame propagation are not symmetric in a complex knot, so the positive and negative helicity generations are not necessarily equal and the total helicity can be generated. In the absence of extinction for $\phi = 0.65$, the flame propagation direction is mainly perpendicular to the vortex centerline, so the helicity generated by the flame propagation is relatively small.

4. Discussion

The 3D flame-vortex interaction in a knotted configuration shows that the helicity can be generated when the flame propagates along the vortex axis. This mechanism can also occur in practical turbulent combustion applications. For instance, the DNS of turbulent premixed combustion showed the coherent fine-scale eddies parallel to local flame fronts [57]. The propagation of flame along the vortex axis was found in the flashback of turbulent premixed flames [58,59]. The interaction between the strong helical vortex and the flame can cause local flame propagation along the vortex axis in swirling turbulent premixed combustion. In these circumstances, the helicity can be generated and the local flow topology and helicity cascade can be affected, which are worth being investigated in future work.

The helicity generation mechanism is not expected to be significantly affected by the chemical modeling. As shown in Sec. III B 3, the helicity is generated when the flame propagates along the vortex axis and causes a local pressure gradient that is not perpendicular to the vortex axis. The flame propagation and combustion heat release, which determine the helicity generation, can be well captured by the one-step chemistry used in the present paper.

C. Flame and vortex morphology

1. Morphology of flame and vortex tubes

As observed in Figs. 3 and 4, the inner portions of both the flame and vortex tubes become flattened, as the flame propagates outward and the vortex tube evolves under self-induction. In the

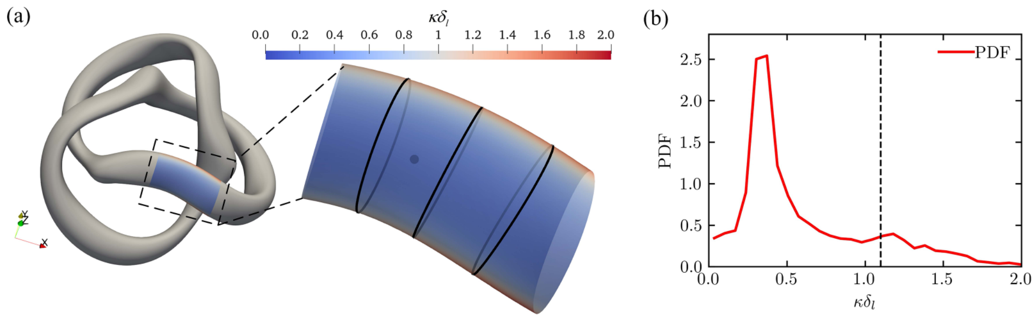

FIG. 10. (a) Extracted flame isosurface marked by a dashed box and color-coded by the normalized curvature $\kappa\delta_l$. The nonextracted surface is in gray. The black solid lines represent cross sections of the flame isosurface normal to its centerline. The gray dot marks a point on the slice plane in the trefoil-knot case in Fig. 13. (b) The PDF of the curvature of the extracted flame isosurface at $t^* = 2$ and with $\phi = 0.65$. The dashed line marks the initial curvature of the flame tube $\kappa = 1/r$ neglecting the curvature of the center axis.

present paper, the morphology of the flame and vortex tubes is analyzed based on the reactive case for $\phi = 0.65$ without local extinction. The morphology of the flame is quantified by the probability density function (PDF) of the curvature $\kappa = -\nabla \cdot \boldsymbol{n}$ with $\boldsymbol{n} = \nabla c/|\nabla c|$ over a part of the flame front. As marked in Fig. 10(a), the extracted part is located within a box defined by $0 \leqslant x/L \leqslant 0.15$, $-0.19 \leqslant y/L \leqslant -0.08$, and $-0.08 \leqslant z/L \leqslant 0.01$, which is relatively smooth and remote from the reconnection sites. In Fig. 10(a), the cross section of the flame tube, which is initially circular with the radius of $\delta_l/r = 1.1$, becomes ellipsoidal at $t^* = 2$. The PDF peak near $\kappa\delta_l = 0.4$ characterizes the flattened flame front, and the long tail of the PDF at large curvature values corresponds to the upper and lower corners of the flame front.

The flattening of vortex and flame tubes in the reactive cases differs from the flattening of vortex cores during the vortex reconnection [12,60]. The latter occurs near the reconnection site where vortex tubes collide, and it becomes more pronounced at higher Re [12]. We find the flattening of the vortex and flame tubes in our DNS is much more apparent in the reactive case, where the local Re is reduced due to the temperature dependence of the viscosity. The flattening occurs long before the reconnection and is significant, remote from the reconnection sites, so it is related to the flame-vortex interaction.

The flame deformation can be caused by the flame propagation and vortex stretch. For a lean methane flame tube, the intrinsic negative-curvature dependence of the flame propagation speed [61] tends to smooth the flame and thus inhibits the evolution towards a flattened tube with highly curved corners. Therefore, the present flame deformation at small Da mainly results from the vortical stretch rather than the curvature-dependent flame propagation.

2. Vortex evolution and baroclinic effects

To explain the flattening of the vortex and flame tubes, the transport equation

$$\underbrace{\frac{\partial \Omega}{\partial t} + u_j \frac{\partial \Omega}{\partial x_j}}_{D\Omega/Dt} = \underbrace{-2\Omega \frac{\partial u_j}{\partial x_j}}_{\text{Dila}} + \underbrace{\omega_i \omega_j \frac{\partial u_i}{\partial x_j}}_{\text{Stretch}} + \underbrace{\frac{1}{\rho^2} \omega_i \varepsilon_{ijk} \frac{\partial \rho}{\partial x_j} \frac{\partial P}{\partial x_k}}_{\text{Baro}} + \underbrace{\omega_i \varepsilon_{ijk} \frac{\partial}{\partial x_j}\left(\frac{1}{\rho}\frac{\partial \tau_{km}}{\partial x_m}\right)}_{\text{Visc}} \tag{23}$$

of the enstrophy in variable-density flows is studied in the reactive case with $\phi = 0.65$, where the four terms on the right-hand side represent the dilatation, stretching, baroclinic torque, and viscous dissipation, respectively. In incompressible flows, the dilatation and baroclinic terms vanish.

Figure 11 plots the volumetric integration of the decomposed budgets of the enstrophy normalized by Γ^3/R_t^3, in the reactive case with $\phi = 0.65$ during the early evolution. The superscripts + and – in Fig. 11 are defined as in Eq. (22). The budget residual is negligibly small. The dilatation

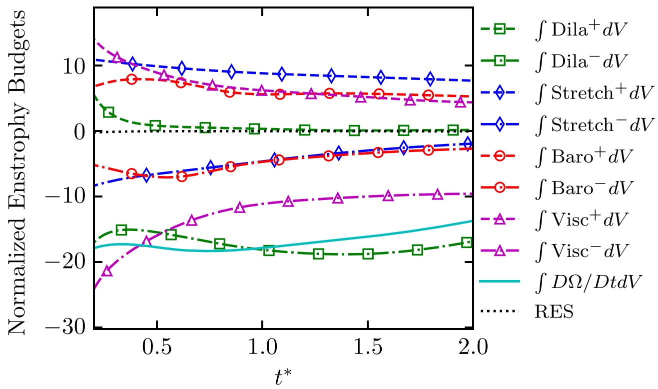

FIG. 11. Volumetric integration of the decomposed enstrophy budgets in the reactive case with $\phi = 0.65$. The residual is evaluated as RES $= \int(D\Omega/Dt$ − Dila − Stretch − Baro − Visc$)dV$.

and viscous terms are mainly negative due to the combustion heat release, leading to the rapid decay of the enstrophy. The positive and negative contributions of the stretching and the baroclinic torque are similar in magnitude and comparable to the positive viscous contribution.

Although the dilatation and the viscous dissipation drive the enstrophy decay, they do not cause the morphological difference of the vortex tubes in reactive and nonreactive cases. This is explained by Fig. 12, which compares distributions of the enstrophy-budget contributions in the reactive case with $\phi = 0.65$ and the nonreactive case at $t^* = 1$. The isosurfaces of the dilatation term and the vorticity are similar, which are initially tubular, so it cannot contribute to the flattening of the vortex tube. The distributions of the stretching term and the viscous dissipation term in the two cases are also similar.

The last possible cause for the vortex tube deformation is the baroclinic term. Its positive parts entangle with the negative parts, especially in the inner portion of the vortex tubes. As depicted in Fig. 13(a), the former lies roughly along the major axis of the elliptical vortex tube, and the latter lies along the minor axis. As illustrated in Fig. 14, this distribution accelerates the flattening of the vortex tube, suggesting that the baroclinic effect plays a key role in the vortex flattening. This mechanism is supported by the similar distributions of $D\Omega/Dt$ and the baroclinic term in the reactive case in Fig. 12. Without the baroclinic contribution, the distribution of $D\Omega/Dt$ in the nonreactive case is governed by the stretch term, and thus the vortex tube is less prone to flattening before reconnection.

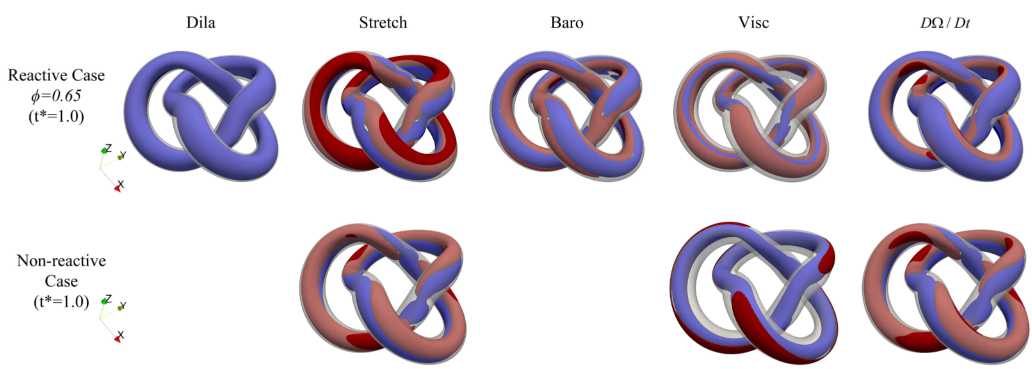

FIG. 12. Contributing terms of the enstrophy budgets along with the material derivative of the enstrophy in the case with $\phi = 0.65$ and the non-reactive case at $t^* = 1$. The red and blue colors denote positive and negative 5% of the maximum value, respectively, and the grey color represents the isosurface of $|\boldsymbol{\omega}^*| = 2$.

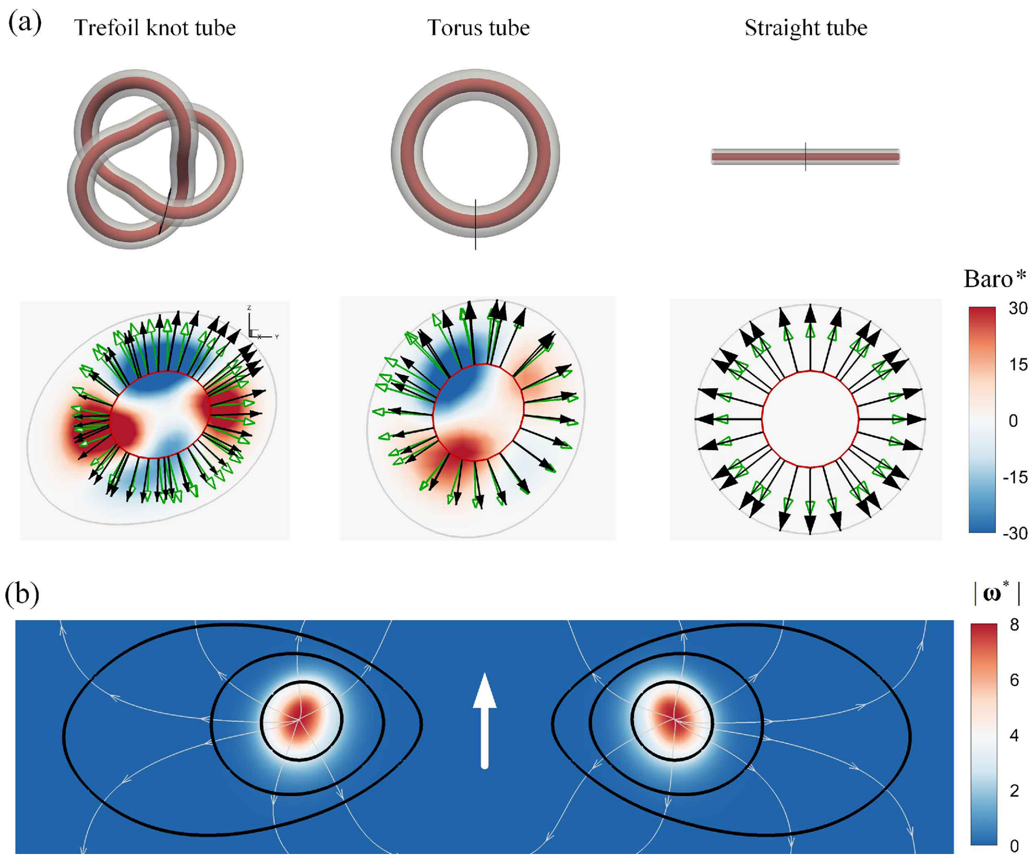

FIG. 13. Configuration effects on the baroclinic term of Eq. (23) and vortex (flame) tube morphology. Upper row of (a): initial configurations with isosurfaces of $|\boldsymbol{\omega}^*| = 2$ (grey) and the flame with $c = 0.5$ (red). Lower row of (a): contour plots of the normalized baroclinic term of Eq. (23) along with isolines of $|\boldsymbol{\omega}^*| = 2$ (grey) and of $c = 0.5$ (red) and vectors of $\nabla\rho$ (green) and ∇p (black) on a cross-sectional slice at $t^* = 0.5$ with different initial configurations. The slices are normal to the vortex axis and are marked by thin black lines in the initial configurations. The slice in the trefoil knot case is extracted near the center of the flame portion in Fig. 10(a). (b) Contour of $|\boldsymbol{\omega}^*|$ along with isolines of p (black) and streamtraces of ∇p (grey lines with arrows) on a slice normal to the vortex axis of the vortex ring with the moving direction marked by the thick arrow.

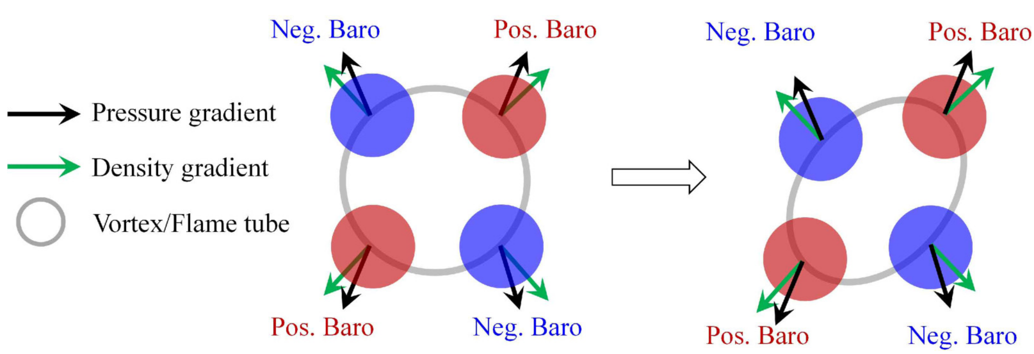

FIG. 14. Illustration of baroclinic torque generation and vortex (flame) tube deformation. Red and blue patches denote positive and negative parts of the baroclinic term, respectively.

The generation of the baroclinic term in Eq. (23) depends on the initial configuration, which is illustrated with the initial trefoil knotted, torus, and straight tubes in Fig. 13. In the three configurations, the vorticity flux and radii of the vortex and flame tubes are the same, respectively. For the initial straight tube, which is essentially a 2D configuration, both the density and pressure gradients are normal to the concentric vortex and flame tubes, so the baroclinic term is vanishing and there is no vortex and flame deformations. For the 3D initial configurations of the ring and knot, the pressure is strongly affected by the nonlocal vortex self-inductions, as illustrated in Fig. 13(b), and thus its gradient misaligns with the density gradient which is locally normal to the flame front. Thus, as shown in Figs. 13 and 14, the positive (red patches) and negative (blue patches) baroclinic terms are generated to stretch and compress the vortex tube in the two orthogonal directions, respectively, resulting in the tube flattening. Due to the dominance of the vortical stretching on the flame shape, the flame tube is also flattened.

3. Discussion

We have highlighted the baroclinic effect caused by the nonlocal pressure distribution in the 3D configuration on vortex (flame) morphology. It differs from previous works on the baroclinic effects in 2D flame-vortex interactions focusing on the vorticity generation [62,63]. The baroclinic torque is relatively weak in generating vorticity at low Da, but it is still important in deforming vortex and flame surfaces. This effect is due to the misalignment of pressure and density gradients caused by the flame propagation. It is not restricted to the specific trefoil knot configuration, as illustrated in Fig. 13, but is also of interest for practical turbulent premixed combustion, where the baroclinic torque arises when the flame propagation interacts with large-scale vortices or with globally swirling, expanding, or diverging flows [64–68]. Since the morphology evolution of vortical structures across different scales is associated with the turbulence cascade [27–29], the combustion effects on the kinetic energy transfer can be elucidated through studying the baroclinic effects on the vortex morphology, which will be investigated in the future work. Additionally, the analysis can be further extended to study the baroclinic effects on the flame wrinkling in realistic configurations with large-scale vortical structures.

In the present trefoil knot configuration, Da is chosen to be close to Da^*, so the flame propagates at a speed similar to that of the vortex evolution and the baroclinic effect is significant. For $\mathrm{Da} \ll \mathrm{Da}^*$, the vortex stretching dominates over the flame propagation and the flame can even be extinguished. For $\mathrm{Da} \gg \mathrm{Da}^*$, the flame burns much faster than the vortex evolves, and the vortex tube quickly dissipates due to the enhanced viscosity. In both cases, the baroclinic torque becomes insignificant to deform the vortex (flame) tube.

IV. CONCLUSIONS

We report a numerical study on the flame-vortex interaction between trefoil knotted vortex and flame tubes in a 3D configuration. The flame is initially located within the vortex tube with the same centerline. In the DNS with parameters determined from the timescale analysis, the flame propagates outward and the vortex evolves under self-induction, along with the flame extinction, flame-flame interaction, and the suppression of vortex reconnection.

The flame-vortex interactions are analyzed through the helicity dynamics and flame (vortex) morphology. We derive the governing equation for H in periodic variable-density flows, and find that the terms related to flame propagation and the viscous effect drive the variation of H. The combustion effect generally diminishes H, whereas causes the helicity growth in a short period due to the flame propagation along the vortex centerline after the local extinction.

Compared to the morphology of the trefoil knotted tube in the nonreactive flow, the flame and vortex tubes are flattened before the vortex reconnection. From the analysis on the enstrophy evolution, we find that the flattening results from the baroclinic effect—the misalignment of the pressure and the density gradients under the 3D configuration and nonlocal pressure effect.

The conclusions on the helicity dynamics and the baroclinic effects have been demonstrated in the proposed 3D trefoil knot configuration. Note that the flame knot appears to be difficult to construct experimentally. Moreover, some of the flame-vortex interaction mechanisms studied in the current configuration could be important in practical combustion, e.g., flame propagation along the vortex axis during swirling flame flashback [59], tubelike structures along the axis of small-scale eddies in premixed turbulent combustion [57], and global pressure gradient in swirling, converging, and diverging flows in combustion [64–66]. In particular, the mechanisms on the helicity cascade, vortex dynamics, and flame wrinkling are expected to be used in the modeling of turbulent premixed combustion.

ACKNOWLEDGMENTS

We gratefully acknowledge Caltech, the University of Colorado at Boulder, and Stanford University for licensing the NGA code used in this work, and thank W. Shen for helpful comments. This work has been supported in part by the National Natural Science Foundation of China (No. 91841302, No. 11925201, and No. 11988102), the Fellowship of China Postdoctoral Science Foundation (No. 2021M700204), the National Key R&D Program of China (No. 2020YFE0204200), and the Xplore Prize.

APPENDIX A: SENSITIVITY TO THE INITIAL FLAME THICKNESS

We investigate the influence of the initial flame thickness δ on the simulation results in the reactive case with $\phi = 0.55$ and $N = 1024$. Figure 15 compares the evolution of the flame surfaces and the isosurfaces of $|\boldsymbol{\omega}|$ with $\delta/\delta_l = 0.065$, 0.13, and 0.26. The initial flame thickness affects the flame quenching and the subsequent flame-vortex interactions. The flame with $\delta/\delta_l = 0.065$ is quenched at $t^* = 2$ and the vortex tube then evolves in a way similar to that in the nonreactive case.

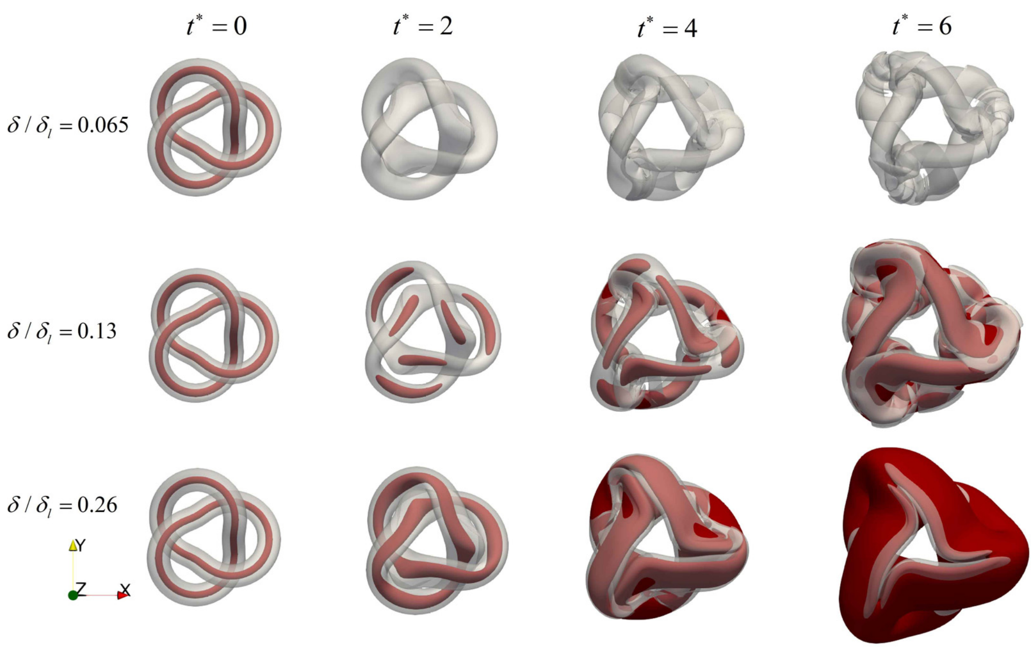

FIG. 15. Evolution of flame fronts represented by isosurfaces of $c = 0.8$ (red) and vortex structures represented by isosurfaces of $|\boldsymbol{\omega}^*|$ (grey) in the reactive case with $\phi = 0.55$ and with $\delta/\delta_l = 0.065$ (upper), $\delta/\delta_l = 0.13$ (middle), and $\delta/\delta_l = 0.26$ (lower). The isocontour values of $|\boldsymbol{\omega}^*|$ are the same as in Fig. 4.

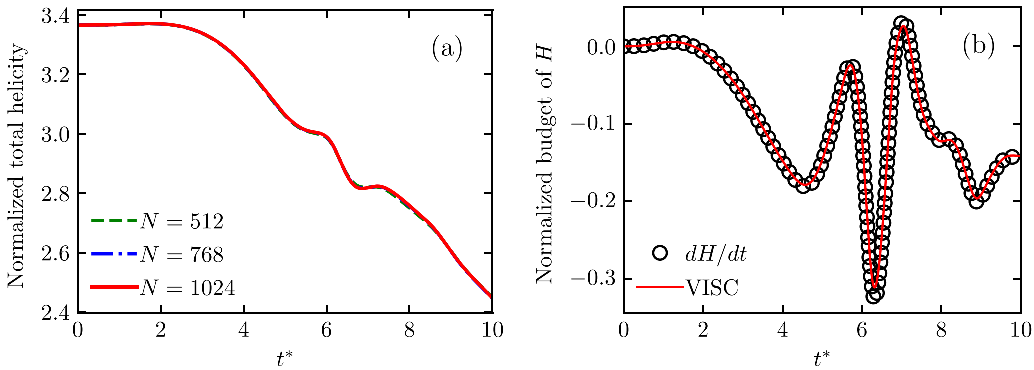

FIG. 16. Grid convergence test for the nonreactive case with $\mathrm{Re} = 2000$. (a) Evolution of H with $N^3 = 512^3$, 768^3, and 1024^3. (b) Helicity budget with $N^3 = 1024^3$.

In contrast, the flame with $\delta/\delta_l = 0.13$ is locally extinguished at $t^* = 2$ and then propagates both outward and along the vortex axis. The flame extinction is not observed for $\delta/\delta_l = 0.26$.

The influence of the initial flame thickness on the quenching results from the dependence of the initial flame propagation speed on δ/δ_l. With the initially reduced flame speed for small δ/δ_l, the vortex straining dominates over the flame propagation, and the flame can be quenched locally or globally in the early stage of the flame-vortex interaction. To study the nontrivial flame-vortex interaction with the flame propagation along the vortex axis, we set $\delta/\delta_l = 0.13$ to realize the local flame extinction in the case of $\phi = 0.55$.

APPENDIX B: GRID CONVERGENCE TEST

The grid convergence test for H has been performed for all DNS cases with grid resolutions $N^3 = 512^3$, 768^3, and 1024^3. Figure 16 shows H converges for $N^3 = 1024^3$ for the nonreactive case with $\mathrm{Re} = 2000$. Moreover, the helicity budget for $N^3 = 1024^3$ examined in Fig. 16(b) shows that dH/dt on the left-hand side of Eq. (20) agrees well with VISC on the right-hand side of Eq. 20 with PRES ≈ 0.

Figure 17 shows the grid convergence test for the two reactive cases. For $\phi = 0.55$, the total helicities obtained with $N^3 = 768^3$ and $N^3 = 1024^3$ are slightly different for $3 < t^* < 5$, possibly due to the grid dependence of the local extinction. For $\phi = 0.65$, H is well converged from $N^3 = 512^3$ to 1024^3. In both the reactive cases, the resolution with $N = 1024$ corresponds to $\Delta/\delta_l = 15$, where Δ denotes the grid size, so it is sufficient to resolve the flame propagation [37,45].

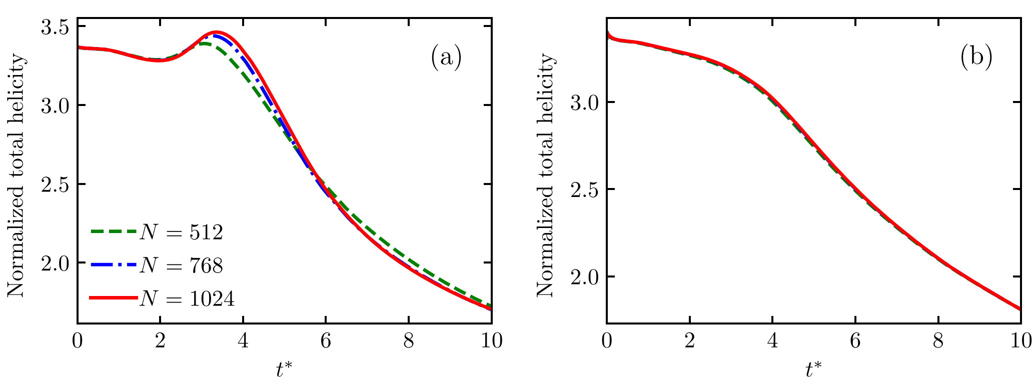

FIG. 17. Grid convergence test for the reactive cases with (a) $\phi = 0.55$ and (b) $\phi = 0.65$.

[1] W. T. Ashurst and P. A. Mcmurtry, Flame generation of vorticity: Vortex dipoles from monopoles, Combust. Sci. Technol. **66**, 17 (1989).
[2] T. Poinsot, D. Veynante, and S. Candel, Quenching processes and premixed turbulent combustion diagrams, J. Fluid Mech. **228**, 561 (1991).
[3] F. Thiesset, F. Halter, C. Bariki, C. Lapeyre, C. Chauveau, I. Gökalp, L. Selle, and T. Poinsot, Isolating strain and curvature effects in premixed flame/vortex interactions, J. Fluid Mech. **831**, 618 (2017).
[4] A. M. Steinberg, K. Teav, S. Kheirkhah, C. Bariki, F. Thiesset, C. Chauveau, and F. Halter, Auto-ignition of near-ambient temperature H_2/air mixtures during flame-vortex interaction, Proc. Combust. Inst. **37**, 2425 (2019).
[5] C. Bariki, F. Halter, F. Thiesset, C. Chauveau, I. Gökalp, K. Teav, S. Kheirkhah, and A. M. Steinberg, Structural response of different Lewis number premixed flames interacting with a toroidal vortex, Proc. Combust. Inst. **37**, 1911 (2019).
[6] C. Meneveau and T. Poinsot, Stretching and quenching of flamelets in premixed turbulent combustion, Combust. Flame **86**, 311 (1991).
[7] F. Charlette, C. Meneveau, and D. Veynante, A power-law flame wrinkling model for LES of premixed turbulent combustion part I: Non-dynamic formulation and initial tests, Combust. Flame **131**, 159 (2002).
[8] S. Lapointe, B. Bobbitt, and G. Blanquart, Impact of chemistry models on flame-vortex interaction, Proc. Combust. Inst. **35**, 1033 (2015).
[9] Y. Zhao, Y. Yang, and S. Chen, Vortex reconnection in the late transition in channel flow, J. Fluid Mech. **802**, R4 (2016).
[10] S. Xiong and Y. Yang, Identifying the tangle of vortex tubes in homogeneous isotropic turbulence, J. Fluid Mech. **874**, 952 (2019).
[11] H. Daryan, F. Hussain, and J.-P. Hickey, Aeroacoustic noise generation due to vortex reconnection, Phys. Rev. Fluids **5**, 062702(R) (2020).
[12] J. Yao and F. Hussain, Vortex reconnection and turbulence cascade, Annu. Rev. Fluid Mech. **54**, 317 (2022).
[13] H. Zhou, J. You, S. Xiong, Y. Yang, D. Thévenin, and S. Chen, Interactions between the premixed flame front and the three-dimensional Taylor-Green vortex, Proc. Combust. Inst. **37**, 2461 (2019).
[14] D. Kleckner and W. T. M. Irvine, Creation and dynamics of knotted vortices, Nat. Phys. **9**, 253 (2013).
[15] S. Xiong and Y. Yang, Construction of knotted vortex tubes with the writhe-dependent helicity, Phys. Fluids **31**, 047101 (2019).
[16] S. Xiong and Y. Yang, Effects of twist on the evolution of knotted magnetic flux tubes, J. Fluid Mech. **895**, A28 (2020).
[17] J. Yao, Y. Yang, and F. Hussain, Dynamics of a trefoil knotted vortex, J. Fluid Mech. **923**, A19 (2021).
[18] J. Yao, W. Shen, Y. Yang, and F. Hussain, Helicity dynamics in viscous vortex links, J. Fluid Mech. **944**, A41 (2022).
[19] W. Shen, J. Yao, F. Hussain, and Y. Yang, Topological transition and helicity conversion of vortex knots and links, J. Fluid Mech. **943**, A41 (2022).
[20] H. K. Moffatt, The degree of knottedness of tangled vortex lines, J. Fluid Mech. **35**, 117 (1969).
[21] M. W. Scheeler, W. M. Van Rees, H. Kedia, D. Kleckner, and W. T. M. Irvine, Complete measurement of helicity and its dynamics in vortex tubes, Science **357**, 487 (2017).
[22] H. K. Moffatt, Helicity in laminar and turbulent flow, Annu. Rev. Fluid Mech. **24**, 281 (1992).
[23] H. K. Moffatt, Helicity and singular structures in fluid dynamics, Proc. Natl. Acad. Sci. USA **111**, 3663 (2014).
[24] E. Levich and A. Tsinober, On the role of helical structures in three-dimensional turbulent flow, Phys. Lett. A **93**, 293 (1983).
[25] Z. Yan, X. Li, C. Yu, J. Wang, and S. Chen, Dual channels of helicity cascade in turbulent flows, J. Fluid Mech. **894**, R2 (2020).
[26] T. Yang, Y. Chi, and P. Zhang, Vortex interaction in triple flickering buoyant diffusion flames, Proc. Combust. Inst. **39**, 1893 (2023).
[27] I. Bermejo-Moreno and D. I. Pullin, On the non-local geometry of turbulence, J. Fluid Mech. **603**, 101 (2008).

[28] Y. Yang, D. I. Pullin, and I. Bermejo-Moreno, Multi-scale geometric analysis of Lagrangian structures in isotropic turbulence, J. Fluid Mech. **654**, 233 (2010).
[29] T. Leung, N. Swaminathan, and P. A. Davidson, Geometry and interaction of structures in homogeneous isotropic turbulence, J. Fluid Mech. **710**, 453 (2012).
[30] N. Fogla, F. Creta, and M. Matalon, Effect of folds and pockets on the topology and propagation of premixed turbulent flames, Combust. Flame **162**, 2758 (2015).
[31] C. K. Law, *Combustion Physics* (Cambridge University Press, Cambridge, 2010).
[32] L. Berger, K. Kleinheinz, A. Attili, and H. Pitsch, Characteristic patterns of thermodiffusively unstable premixed lean hydrogen flames, Proc. Combust. Inst. **37**, 1879 (2019).
[33] D. Veynante and L. Vervisch, Turbulent combustion modeling, Prog. Energy Combust. Sci. **28**, 193 (2002).
[34] T. Zheng, J. You, and Y. Yang, Principal curvatures and area ratio of propagating surfaces in isotropic turbulence, Phys. Rev. Fluids **2**, 103201 (2017).
[35] J. You and Y. Yang, Modelling of the turbulent burning velocity based on Lagrangian statistics of propagating surfaces, J. Fluid Mech. **887**, A11 (2020).
[36] M. Matalon, Intrinsic flame instabilities in premixed and nonpremixed combustion, Annu. Rev. Fluid Mech. **39**, 163 (2007).
[37] Y. Su, Z. Lu, and Y. Yang, Suppression of the turbulent kinetic energy and enhancement of the flame-normal Reynolds stress in premixed jet flames at small Lewis numbers, Combust. Flame **246**, 112461 (2022).
[38] R. A. C. Griffiths, J. H. Chen, H. Kolla, R. S. Cant, and W. Kollmann, Three-dimensional topology of turbulent premixed flame interaction, Proc. Combust. Inst. **35**, 1341 (2015).
[39] A. Tyagi, I. Boxx, S. Peluso, and J. O'connor, Pocket formation and behavior in turbulent premixed flames, Combust. Flame **211**, 312 (2020).
[40] Y. Minamoto, B. Yenerdag, and M. Tanahashi, Morphology and structure of hydrogen-air turbulent premixed flames, Combust. Flame **192**, 369 (2018).
[41] O. Chatakonda, E. R. Hawkes, A. J. Aspden, A. R. Kerstein, H. Kolla, and J. H. Chen, On the fractal characteristics of low Damköhler number flames, Combust. Flame **160**, 2422 (2013).
[42] D. Veynante and V. Moureau, Analysis of dynamic models for large eddy simulations of turbulent premixed combustion, Combust. Flame **162**, 4622 (2015).
[43] S. Xiong and Y. Yang, Evolution and helicity analysis of linked vortex tubes in viscous flows, Sci. Sin.: Phys. Mech. Astron. **50**, 040005 (2019).
[44] X. Zhao and C. Scalo, Helicity dynamics in reconnection events of topologically complex vortex flows, J. Fluid Mech. **920**, A30 (2021).
[45] S. H. Kim and Y. Su, Front propagation formulation for large eddy simulation of turbulent premixed flames, Combust. Flame **220**, 439 (2020).
[46] S. Nishiki, T. Hasegawa, R. Borghi, and R. Himeno, Modeling of flame-generated turbulence based on direct numerical simulation databases, Proc. Combust. Inst. **29**, 2017 (2002).
[47] T. Kulkarni, R. Buttay, M. H. Kasbaoui, A. Attili, and F. Bisetti, Reynolds number scaling of burning rates in spherical turbulent premixed flames, J. Fluid Mech. **906**, A2 (2021).
[48] O. Desjardins, G. Blanquart, G. Balarac, and H. Pitsch, High order conservative finite difference scheme for variable density low Mach number turbulent flows, J. Comput. Phys. **227**, 7125 (2008).
[49] S. H. Kim, Leading points and heat release effects in turbulent premixed flames, Proc. Combust. Inst. **36**, 2017 (2017).
[50] J. F. MacArt, T. Grenga, and M. E. Mueller, Effects of combustion heat release on velocity and scalar statistics in turbulent premixed jet flames at low and high Karlovitz numbers, Combust. Flame **191**, 468 (2018).
[51] Y. Su and S. H. Kim, An improved consistent, conservative, non-oscillatory and high order finite difference scheme for variable density low Mach number turbulent flow simulation, J. Comput. Phys. **372**, 202 (2018).
[52] G.-S. Jiang and C.-W. Shu, Efficient implementation of weighted ENO schemes, J. Comput. Phys. **126**, 202 (1996).

[53] C. D. Pierce, Progress-variable approach for large-eddy simulation of turbulent combustion, Ph.D. thesis, Stanford University, 2001.
[54] X. Zhao, Z. Yu, J.-B. Chapelier, and C. Scalo, Direct numerical and large-eddy simulation of trefoil knotted vortices, J. Fluid Mech. **910**, A31 (2021).
[55] P. E. Lapenna, R. Lamioni, G. Troiani, and F. Creta, Large scale effects in weakly turbulent premixed flames, Proc. Combust. Inst. **37**, 1945 (2019).
[56] Y. Levy, D. Degani, and A. Seginer, Graphical visualization of vortical flows by means of helicity, AIAA J. **28**, 1347 (1990).
[57] M. Tanahashi, M. Fujimura, and T. Miyauchi, Coherent fine-scale eddies in turbulent premixed flames, Proc. Combust. Inst. **28**, 529 (2000).
[58] E. Tangermann, M. Pfitzner, M. Konle, and T. Sattelmayer, Large-eddy simulation and experimental observation of combustion-induced vortex breakdown, Combust. Sci. Technol. **182**, 505 (2010).
[59] J. Fritz, M. KröNer, and T. Sattelmayer, Flashback in a swirl burner with cylindrical premixing zone, J. Eng. Gas Turbines Power **126**, 276 (2004).
[60] A. Pumir and R. M. Kerr, Numerical simulation of interacting vortex tubes, Phys. Rev. Lett. **58**, 1636 (1987).
[61] N. Peters, *Turbulent Combustion* (Cambridge University Press, Cambridge, 2000).
[62] C. J. Mueller, J. F. Driscoll, D. L. Reuss, M. C. Drake, and M. E. Rosalik, Vorticity generation and attenuation as vorticies convect through a premixed flame, Combust. Flame **112**, 342 (1998).
[63] D. Louch and K. Bray, Vorticity and scalar transport in premixed turbulent combustion, Symp. (Int.) Combust. **27**, 801 (1998).
[64] A. Kazbekov, K. Kumashiro, and A. M. Steinberg, Enstrophy transport in swirl combustion, J. Fluid Mech. **876**, 715 (2019).
[65] M. K. Geikie and K. A. Ahmed, Pressure-gradient tailoring effects on the turbulent flame-vortex dynamics of bluff-body premixed flames, Combust. Flame **197**, 227 (2018).
[66] B. A. Ochs, R. Ranjan, D. Ranjan, and S. Menon, Topology and flame speeds of turbulent premixed flame kernels in supersonic flows, Combust. Flame **210**, 83 (2019).
[67] A. Kazbekov and A. M. Steinberg, Influence of flow structures and combustion on cross-scale turbulent kinetic energy transfer in premixed swirl flames, Proc. Combust. Inst. **39**, 2329 (2023).
[68] S. H. R. Whitman, T. J. Souders, M. A. Meehan, J. G. Brasseur, and P. E. Hamlington, Pressure gradient tailoring effects on vorticity dynamics in the near-wake of bluff-body premixed flames, Proc. Combust. Inst. **39**, 2359 (2023).